Journal of Materials Chemistry C

ROYAL SOCIETY OF CHEMISTRY

PAPER

Check for updates

Cite this: J. Mater. Chem. C, 2023, 11, 7451

The impact of side chain elongation from the Y6 to Y6-12 acceptor in organic solar cells: a fundamental study from molecules to devices†

Florian Regnier,[ab] Antoine Rillaerts,[ab] Vincent Lemaur,[a] Pascal Viville*[b] and Jérôme Cornil*[a]

Received 22nd February 2023, Accepted 3rd May 2023

DOI: 10.1039/d3tc00666b

rsc.li/materials-c

In order to contribute to the establishment of clear structure–property relationships of non-fullerene acceptors in organic solar cells, we focus here on the rising star Y6 acceptor to assess the impact of elongating the inner side chain from 8 to 12 carbon atoms *via* a joint theoretical and experimental characterization study combining DFT calculations, UV-visible spectroscopy, atomic force microscopy (AFM) analysis and device fabrication and characterization. The originality of the present work is to compare Y6 and Y6-12 under the same experimental conditions in order to make more transparent the added benefits of using longer saturated side chains. Although the optoelectronic properties of the blends with the prototypical PM7 donor polymer are not strongly impacted by the side chain length, the morphology of the films is deeply modified as a function of the nature of the solvent used for their processing, which affects in turn the performance of the devices.

1. Introduction

In recent years, the field of organic electronics has been receiving extensive attention from the scientific community and has transformed into a commercial success in the case of organic light-emitting diodes (OLEDs). Another key application under intense scrutiny is the development of organic photovoltaic devices (OPVs), as prompted by several attractive features such as light weight,[1–3] good mechanical flexibility,[1–3] large area coating with low material consumption ($\sim$1 g m^{-2})[3], solution processability[4], which could make them part of the solution to fight against the current climatic changes and energy crisis[2,5].

In deep analogy with the p–n junctions in silicon-based solar cells, a bulk-heterojunction (BHJ) organic solar cell is made from a homogeneous mixing of an electron donating material and an electron accepting material[1,5,6] typically sandwiched between two metallic electrodes.[7–9] The global working principle of a BHJ solar cell can be divided into 5 main steps that must be each optimized, see Fig. 1: (1) photon absorption and electron–hole pair (exciton) generation; (2) exciton diffusion towards a donor–acceptor interface; (3) charge-transfer state formation and its dissociation into free charge carriers; (4) transport of charges towards the electrodes; (5) selective charge collection at each electrode.[6,10,11] In order to facilitate charge transport and charge collection to the electrodes, ultrathin inorganic or organic intermediate layers can be introduced in the device structure.[6,12–14] Another role of these extra layers is to prevent recombination of excitons at the electrode, to block selectively holes at the cathode and electrons at the anode[6,14,15] and to prevent damaging chemical reactions or ion diffusion at the electrode/organic interface,[6,15] thus helping to increase the stability and hence the lifetime of the devices.

The first generation of OPVs was typically based on donor polymers combined with the prototypical solution processible n-type fullerene acceptor molecule 1-(3-methoxycarbonyl)-propyl-1-phenyl-[6,6]C_{61}/C_{71} ($PC_{61}BM$ or $PC_{71}BM$).[1,16,17] Such devices led to conversion efficiencies in a typical range between 5 and 11%[16,18] but suffered from the poor absorption properties of fullerenes, chemical stability problems and morphological instability linked to the spherical shape of the fullerene compounds.[2,10,17,19]

The field of organic photovoltaics has clearly experienced a second birth with the introduction of non-fullerene acceptor molecules (NFAs) such as the ITIC-series followed by the Y-series (see Fig. 2), associated with new matching donor polymers.[1,2]

This new class of acceptor molecules typically exhibits a global A–D–A (acceptor–donor–acceptor) or an A–D–A′–D–A

[a] Laboratory for Chemistry of Novel Materials, University of Mons, B-7000 Mons, Belgium. E-mail: Jerome.CORNIL@umons.ac.be, Florian.REGNIER@umons.ac.be, Antoine.RILLAERTS@umons.ac.be, Vincent.LEMAUR@umons.ac.be

[b] Materia Nova, Research and Development Center, B-7000 Mons, Belgium. E-mail: pascal.viville@interreg-fwvl.org

† Electronic supplementary information (ESI) available. See DOI: https://doi.org/10.1039/d3tc00666b

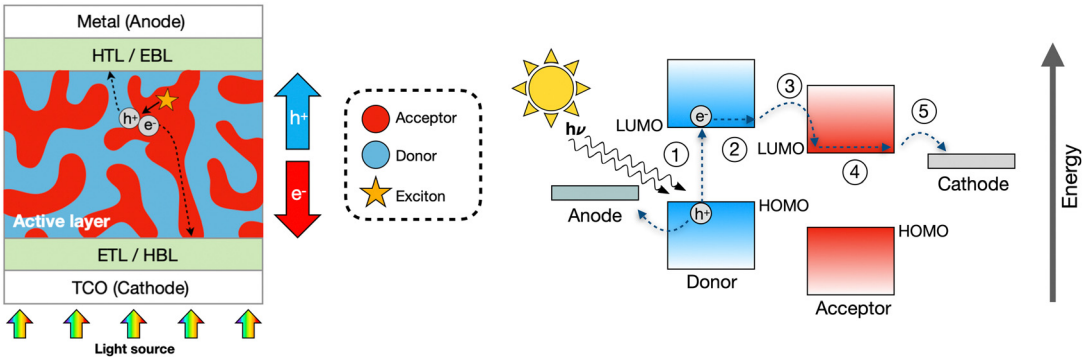

Fig. 1 Architecture of inverted BHJ organic solar cells (A) and its working principle (B). HTL [HBL] stands for the hole transport [blocking] layer and *vice versa* for electrons.

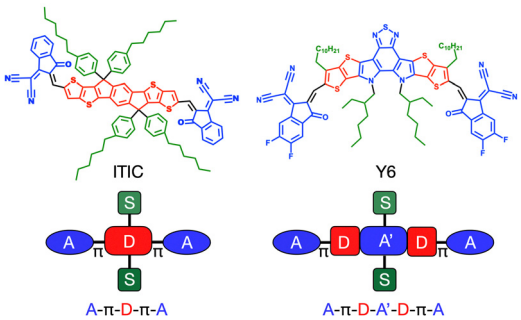

Fig. 2 Molecular structure of ITIC and Y6 NFA. The distinctive domains are highlighted: acceptor unit (blue), donor unit (red) and side chains (green).

molecular structure to create a strong internal push–pull character,[10,18,20,21] and thus a pronounced charge transfer in the excited states which may help in breaking apart the electron–hole pairs.[22] Among them, the acceptor molecule BTP-4F, also referred to as Y6, clearly emerges as a rising star. Its molecular backbone is made of three distinctive parts including (i) a central electron-accepting (core) unit made of a benzothiadiazole unit (BT) fused to two pyrrole rings; (ii) electron-accepting terminal groups separated from the core group by two fused electron-donating thiophene rings; and (iii) lateral side chains.[1,10,20]

To date, NFAs have pushed the power conversion efficiency (η or PCE) to values often above 15% on a lab scale,[2,16,20] after full device optimization and adequate choice of additives. Besides stability issues, NFAs have also the advantage to absorb significantly the solar emission and to have a very modular structure, in contrast to fullerene derivatives, which allows for fine tuning of the solid-state packing and electronic/optical properties driving the efficiency of the different steps of solar conversion.[2,10,17,19,23] Developing new materials with enhanced performance definitively requires the establishment of structure–property-device performance that is most often overlooked when searching for formulations yielding the highest power conversion efficiency or when comparing different materials under different experimental conditions.

In order to vary the electronic and optical properties of the individual molecules, chemical modifications can be brought to the central core or end groups. For example, by extending the number of fused aromatic rings forming the core, the optical gap of the material can be progressively reduced and the frontier electronic levels shifted.[20,24,25]

Modulating the strength of the terminal electron-accepting units is another lever to further tailor the electronic structure.[1,7,10,26–28] For a given backbone, modifying the chemical nature or topology of the saturated side chains will not generally affect the electronic properties of the individual molecules[10,28] but will most often induce significant morphological changes to reduce steric effects and/or optimize van der Waals interactions;[1,7,10,16,28–30] the latter will likely impact the optical properties of the thin films as well as the efficiency of intermolecular processes such as exciton diffusion, exciton dissociation, charge transport, and thus the overall device performance.

The side chains in NFAs can be categorized into two classes: the inner *versus* outer side chains.[30,31] The first group plays a critical role in the solubility of the molecules and molecular packing.[1,30] Long side chains are preferred to improve the solubility[1,32,33] though an excessive length can promote a large separation of the conjugated cores in the solid phase, which constitutes an obstacle for charge transport between molecules. The outer chains can further tune the torsional angles between the central rigid core and the end-groups[1,30,34] by playing with their attachment site, their length, and branching.[10,34–36] For instance, in the study carried out on the Y6 molecule by Jiang and co-workers, swapping the terminal alkyl side chains attached to the thiophene rings in the β position with the 2-ethylhexyl central chains attached on pyrroles leads to reduced solubility and a less favorable morphology compared to the pristine Y6 acceptor, thus decreasing the device performance.[35] Recently, other studies based on polymeric PBDB-T derivatives mixed with a series of different NFAs (IT4F, ITIC and Y6) suggest that modifications in the side chain length can also modulate the spacing between the donor and acceptor molecules, thus impacting interfacial charge transfer and recombination effects (V_{loss}), and by extension the V_{OC} parameter.[37]

 This journal is © The Royal Society of Chemistry 2023

Nevertheless, although side chain engineering is an important research direction, some experimental trends observed are not yet completely understood and some design rules to connect the design of side chains to OPV performances are still missing.

In this context, we report here a fundamental comparative study of the electronic, optical, and morphological properties of Y6 (M_W = 1451.93 Da) *versus* its derivative Y6-12 with longer inner side chains (M_W = 1564.14 Da) under the same experimental conditions to assess the impact of elongating the inner side chain from 8 to 12 carbon atoms. Our joint theoretical and experimental characterization study includes DFT calculations, UV-visible spectroscopy, atomic force microscopy (AFM) analysis and device fabrication and characterization. Both acceptors have been blended with the chlorinated D–A type polymer PM7 ($M_W \sim$ 70–100 kDa) to fabricate solar cells; note that the use of the PM7 polymer instead of the more popular fluorinated derivative (PM6) is not expected to introduce significant changes in the blend properties. Film processing has been carried out from chloroform and chlorobenzene, the two solvents widely used in the literature for dissolving organic semiconductors.[16] The structures of both acceptor NFAs and the donor polymer are shown in Fig. 3. It is worth stressing that our work aims to be very fundamental in nature by comparing Y6 and Y12 under exactly the same experimental conditions (*i.e.*, solvent used, donor/acceptor ratio, and no additives). Such insight cannot be gained in our view when searching for each derivative for the optimized conditions to maximize the power conversion efficiency. This justifies why the PCEs obtained in this work are, though quite decent, not close to the best reported values in the field. Additionally, using an inverted structure has the merit to limit the degradation of the active layers typically observed when using PEDOT-PSS.

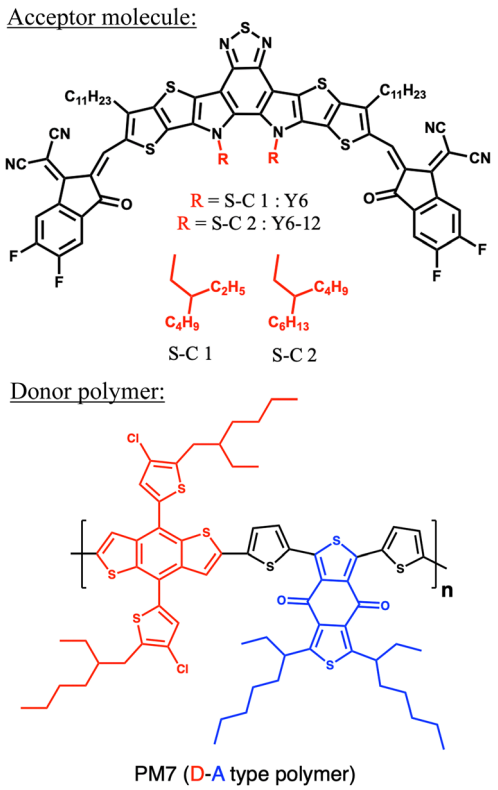

Fig. 3 Structure of NFAs (Y6, Y6-12) and polymer (PM7) involved in this work.

2. Results and discussion

2.1. Theoretical considerations

Although the side chain modulation is not expected to affect the properties of isolated molecules (*i.e.*, in solution), we wanted to start this fundamental study by providing a thorough quantum-chemical description of the electronic levels and excited-states of the Y6 backbone, not readily accessed at the experimental level.

The electronic and optical properties of Y6 have been computed here at the DFT (Density Functional Theory) level using the ω-tuned LC-ωHPBE functional[38–40] and a 6-31G(d,p) basis set, with the Gaussian 16 revision A.03 package.[41] To reduce the calculation time, all alkyl chains were replaced by CH_3 groups[26,42] since it is clearly not here that the actual size of saturated chains will make a strong difference, as also evidenced later on experimentally. The optimized molecular geometry of Y6 was obtained with an adjusted ω of 0.1068 Bohr^{-1} is presented in Fig. 4-A. The molecule is globally planar, except for a slight N–C–C–N torsion angle of 12.7° caused by steric hindrance between the inner CH_3 groups, which is consistent with ωB97X-D/6-31+G(d,p) DFT calculations conducted by Yuan *et al.*[26] This coplanarity is also likely enhanced by the S–O Coulombic attractive interaction ($d_{S-O} \sim$ 2.7 Å) which can trigger conformational blocking.[28,29] The shape of the frontier orbitals has also been computed while considering the solvent effects of chloroform (ε = 4.71) and chlorobenzene (ε = 5.69) *via* the Polarizable Continuum Model (PCM).[43–45]

The wavefunction distributions of the orbitals are similar in both solvents and are displayed in Fig. 4B. In contrast to many donor–acceptor copolymers[46], the LUMO is delocalized over the whole backbone (∼34% on each terminal group) while the HOMO level is mainly localized on the core (∼78%), in agreement with previous data.[42,47] The pronounced LUMO delocalization is *a priori* favorable for intermolecular electron transport by promoting a significant overlap between the LUMO of adjacent molecules. Moreover, such localization patterns indicate that the first excited state, mostly described by a HOMO to LUMO transition, will exhibit significant charge transfer character, which may contribute to intramolecular predissociation of the exciton. The overlap factor (ϕ_S) between the hole and the electron density in the lowest excited state has been estimated at 0.62 in both solvents.[47,48] This points to a good compromise between a charge transfer character ($\phi_S \rightarrow 0$) which facilitates exciton dissociation and a local character allowing for significant optical absorption ($\phi_S \rightarrow 1$).[48] Interestingly, the spatial distribution of the orbitals on the benzothiadiazole unit (BT) represents ∼25% of the weight in the HOMO and ∼5% in the LUMO. This indicates that the BT group alone does not act as a

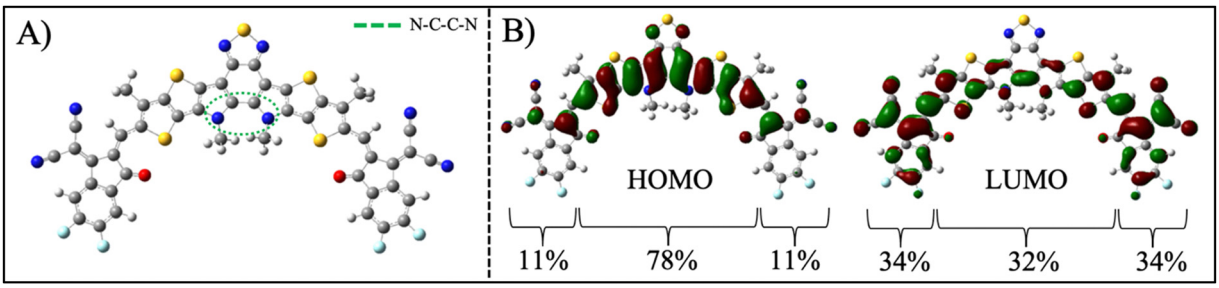

Fig. 4 Optimized structure of Y6 (A) and HOMO/LUMO wavefunction distribution in Y6 (B) obtained from LC-ωHPBE/6-31G(d,p) DFT calculations. The wavefunction sign is represented by red (positive) and green (negative) colors.

good acceptor in Y6. By considering in addition the pyrrole groups attached to the BT unit, the weight of the LUMO and HOMO over the fragment becomes 8% and 50%, respectively.

To further describe the charge distribution in Y6, a Mulliken charge population analysis has been conducted, see Fig. 5. The total atomic charge carried by one terminal group together with the attached π-spacer is about −0.2 |*e*| while it is +0.4 |*e*| for the central core. However, the BT group alone exhibits a positive atomic charge of +0.5 |*e*|, thus demonstrating its weak acceptor character compared to the external electron-accepting units. Taking into account the neighboring fused pyrrole rings, the total atomic charge raises up to −0.66 |*e*|, thus demonstrating that the acceptor character of the central part (A′) is not governed only by the BT unit, as often reported in the literature.[18,21] Additional calculations have been performed on the Y6 molecule with an excess electron *versus* excess hole. Doing so, the Mulliken charge population analysis shows that the BT group alone carries a positive charge of +0.685 |*e*| in the singly positively charged system. When the neighboring pyrrole rings are included, the Mulliken charge becomes −0.751 |*e*| in the negatively charged system. These results confirm the poor acceptor character of the BT group alone in Y6. Moreover, the Mulliken analysis also confirms the possible attractive interaction between the charge on the sulfur atom of one thiophene of the core (+0.38 |*e*|) and that of the adjacent oxygen located on the terminal group (−0.47 |*e*|). The charge distribution over the bent Y6 molecule creates a small permanent dipole moment (μ_{dip}) of 1.7 D along the *Z*-axis direction. This dipole can represent a driving force for molecular packing in films but could also create a significant energetic disorder in more amorphous films, leading to charge recombination *via* the formation of traps, and thus an increase in the energy loss.

Finally, Fig. 6 shows the simulated absorption spectra of Y6 in chloroform and chlorobenzene at the TD-DFT LC-ωHPBE/6-31G(d,p) level, with a full width at half-maximum (FWHM) set at 0.25 eV for the absorption bands.

The global shape is very similar to the simulated spectrum obtained by Yong Cui *et al.*[42] The main absorption peak corresponding to the $S_0 \rightarrow S_1$ transition is located at 625 nm (1.98 eV), with an oscillator strength ($\mathcal{F}$) of 1.8 and a calculated molar absorption coefficient (ε_{mol}) of 1.01×10^5 M^{-1} cm^{-1}. A second absorption peak is also observed at 437 nm and corresponds to the $S_0 \rightarrow S_8$ transition ($\mathcal{F}$ = 0.4 and ε_{mol} = 4.3×10^4 M^{-1} cm^{-1}). Note that the energy of the lowest absorption band is strongly blue-shifted with respect to the corresponding experimental absorption spectra (∼0.29 eV). Nevertheless, an interesting observation is a lack of solvatochromism (∼0.02 eV) predicted by the calculations in spite of the presence of a pronounced internal push–pull character in the molecule, probably due to the fact that the two dipoles point in opposite directions and cancel each other.

The Natural Transition Orbitals (NTO)s for these two optical transitions are displayed in the ESI† (S1); they represent effective orbitals obtained by a weighted average of the different electronic excitations involved in the description of the state.[39]

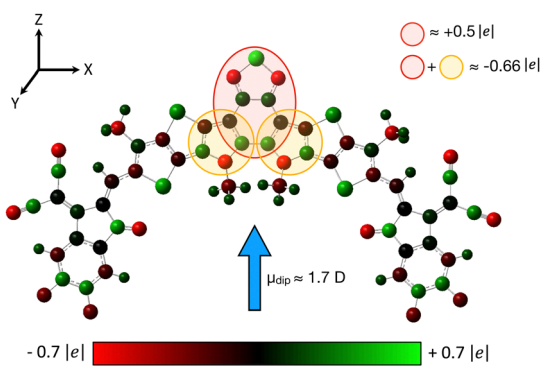

Fig. 5 Mulliken population analysis for the Y6 molecule, as obtained using LC-ωHPBE/6-31G(d,p) DFT calculations.

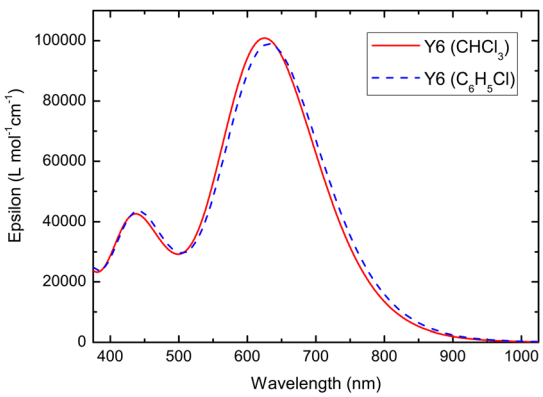

Fig. 6 Simulated absorption spectra obtained from TD-DFT/LC-ωHPBE/6-31G(d,p) calculations for Y6 in chlorobenzene and chloroform.

 This journal is © The Royal Society of Chemistry 2023

As expected, the hole density (ρ_h) and electron density (ρ_e) for $S_0 \rightarrow S_1$ transition have localization similar to the corresponding frontier orbitals since this transition is primarily described by a HOMO → LUMO transition.[39]

2.2. Optical properties

The UV-vis-NIR normalized absorption spectra of the acceptor molecules Y6 and Y6-12 and of the donor polymer PM7 in chloroform (CF) and chlorobenzene (CB) are displayed in Fig. 7 (see S2 for sample preparation and characterization details, ESI†). The maximum of the lowest absorption band peaks for Y6, Y6-12 and PM7 are located at 732 nm (1.69 eV), 733 nm (1.69 eV) and 604 nm (2.05 eV) in CF, respectively while it is situated at 729 nm (1.70 eV), 728 nm (1.70 eV) and 605 nm (2.04 eV) in CB. Note that all optical signatures in CF are consistent with those published in the literature.[21,49]

For all systems, the spectra reflect the absence of a significant solvatochromic effect, as predicted by our theoretical calculations on the acceptor molecule. Since the two acceptor compounds differ by the length of the saturated side chains appended to the nitrogen atom, we obtain as expected the same absorption spectrum for Y6 and Y6-12. From Beer–Lambert's law ($A_\lambda = \varepsilon_\lambda \cdot L \cdot C$)[50,51] with A_λ is the absorbance value at a given wavelength, L is the optical path length (cm) and C is the molar concentration of the absorbing species in solution (mol L^{-1} or M), and the molar absorption coefficients (ε_{max}) at λ_{max} were determined to be 1.75×10^5 M^{-1} cm^{-1} and 1.47×10^5 M^{-1} cm^{-1} for Y6 and Y6-12 respectively, in deep consistency with the theoretical estimates yielding values around 10^5 M^{-1} cm^{-1}. This further demonstrates the very good absorption properties of these compounds compared to fullerene derivatives ($\varepsilon < 0.5 \times 10^5$ M^{-1} cm^{-1})[52] and their strong complementarity with the absorption spectrum of the donor to cover the solar emission range.

The absorption spectrum of each component, presented in Fig. 8, exhibits a red shift when going from solution to a thin film. However, a very small shift of 3 nm (0.01 eV) is observed for PM7 in both solvents whereas Y6 reveals unexpectedly large bathochromic shifts of 87 nm (0.18 eV) and 119 nm (0.24 eV) in CF and CB, respectively; the corresponding values are 81 nm (0.17 eV) and 94 nm (0.19 eV) for Y6-12, respectively. The slightly different amplitudes of this red shift when varying the solvent or the side chain length most likely reflect different molecular arrangements in the thin films driven by the different volatility of the solvents and/or steric effects linked to the side chains[53].

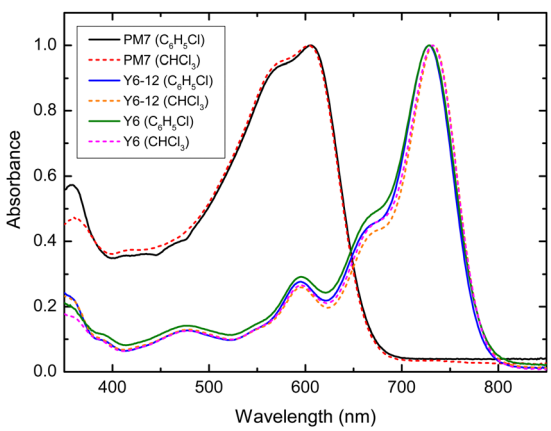

Fig. 7 Normalized absorption spectra of Y6, Y6-12 and PM7 in CF and CB solutions (C = 6.25 10^{-3} mg mL^{-1}).

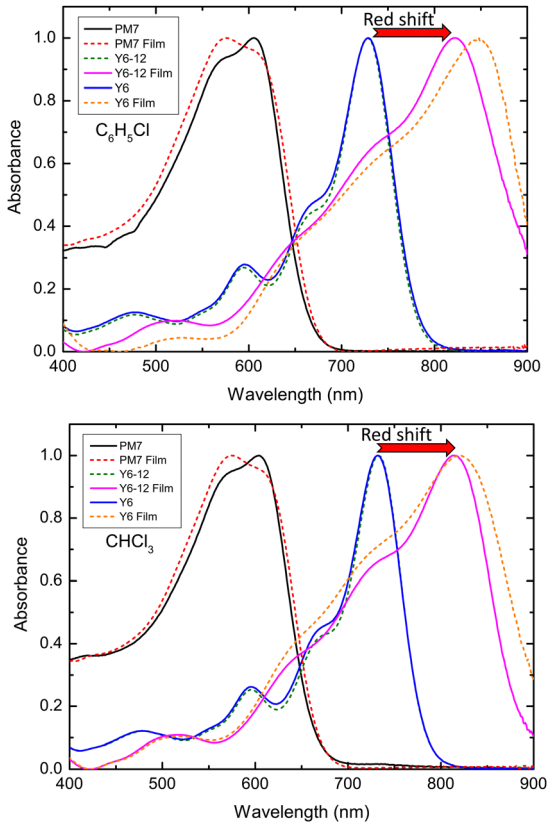

Fig. 8 Absorption spectra of PM7, Y6 and Y6-12 in solution and film prepared from chlorobenzene (upper figure) and chloroform (lower figure).

Red shifts are typically observed for polymers when going from solution to thin films and are typically dominated by planarization of the molecular backbone due to solid-state packing effects[54–56] or to the diffusion of excitations towards the most conjugated segment (*i.e.*, with the lowest optical gap).[57] In our case, the PM7 polymer exhibits two rigid conjugated groups linked together by one thiophene group. Moreover, Coulomb interactions between the sulfur atom of this thiophene ring and the adjacent carbonyl group are expected to lock the chain in a planar conformation. These two features are thus consistent with the fact that the absorption spectra are very similar in solution and in thin films. For Y6, the large red shift observed in the solid state can be inferred either to the formation of molecular J aggregates favoring the delocalization of excitons[55,58] or to a strong impact of electrostatic interactions (due to the local dipoles) modulating the energies of the frontier electronic levels, and hence the optical gap of the individual molecules[59]. Nevertheless, it is striking to observe

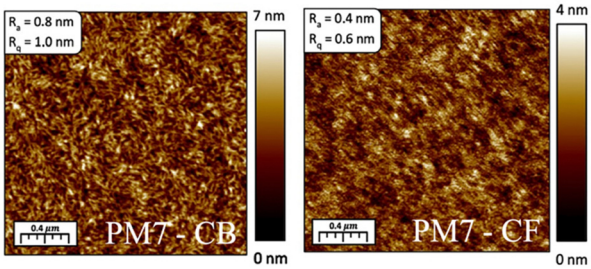

Fig. 9 AFM images (2 × 2 μm^2) for PM7 pure films prepared from chlorobenzene (A) and chloroform (B). Their thickness are 150 nm and 170 nm, respectively.

a very similar red shift for both Y6 and its long-chain derivative Y6-12 whatever the solvent used. This would therefore indicate if aggregation effects prevailed that the latter is not affected by the size of the lateral chains and by the different morphology of the films revealed by AFM, which is rather unexpected. On the other hand, the presence of a permanent dipole moment in Y6 is consistent with the presence of long-range electrostatic effects even in a crystalline structure.

The absorption coefficients in films were determined from the formula $\alpha = \frac{1}{d}\ln\left(\frac{1}{T}\right)$, where d represents the film thickness (cm) and T represents the transmittance.[60] Doing so, the absorption coefficient in neat films was estimated to be 2.81×10^5 cm^{-1} and 2.92×10^5 cm^{-1} for Y6 and Y6-12, respectively.[42] Such high absorption coefficients and the broad absorption band of both NFAs in the 600–900 nm range are highly beneficial for effective solar photon absorption, which should translate into high photocurrent in OSCs.[42]

2.3. Morphological properties

In the next step, Atomic Force Microscopy (AFM) was used to investigate first the surface morphology of non-annealed pure films (PM7, Y6, Y6-12) and non-annealed blend films with a (1 : 1) weight ratio (PM7 : Y6, PM7 : Y6-12), all prepared from either CB and CF solutions (see S2 for experimental details, ESI†). The chosen (1 : 1) ratio is typically used in the literature[2] and thus constitutes a reasonable choice for our fundamental study.

As shown in Fig. 9, the PM7 polymer film exhibits in both solvents a similar smooth surface morphology, with a root mean square surface roughness (R_q) of 1.0 nm in CB and 0.6 nm in CF. A significant degree of organization is evidenced by the presence of 30–70 nm-long fiber-like aggregates, as also reported by Lijiao Ma *et al.*[61,62]

In contrast, the AFM image of the Y6 neat film (Fig. 10A) exhibits in both solvents large domains with a size of 40–110 nm. As a result, the R_q values of the films are much higher, *i.e.*, 5.1 nm in CB and 2.8 nm in CF. Concerning the Y6-12 films (Fig. 10B), much fewer aggregates are observed compared to its counterpart Y6 and the surface appears very smooth, with a R_q of 0.4 nm in CB and 0.3 nm in CF. These results suggest that Y6 molecules have a strong tendency to agglomerate compared to Y6-12, regardless of the solvent used for film processing. This can be rationalized by the fact that longer chains promote better solubility, and hence less pre-aggregation of Y6-12 in both solvents[63]; moreover, they are expected to introduce more steric effects that should limit aggregation in the films.[2]

The AFM images of 100 nm-thick PM7 : Y6 (1 : 1) blend films processed from CB (Fig. 11A) show a granular morphology similar to that visualized for the neat Y6 film, with a high R_q

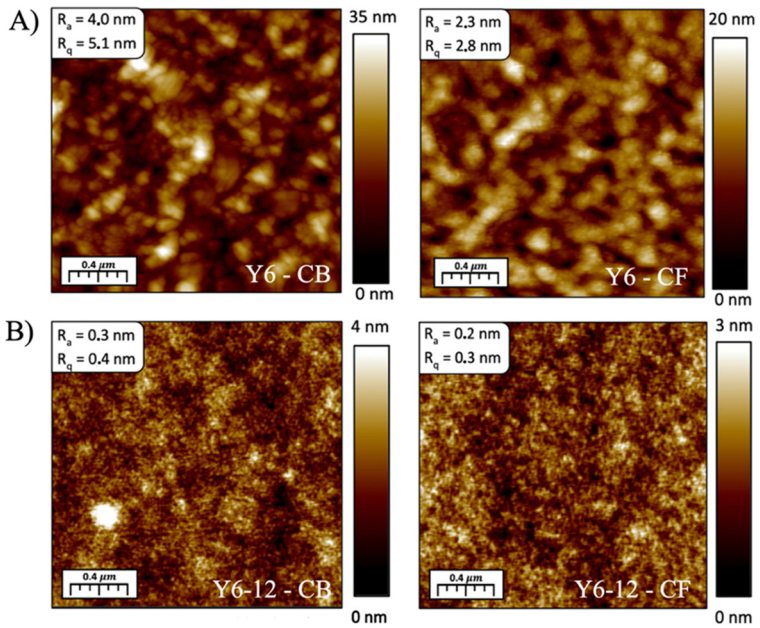

Fig. 10 AFM images (2 × 2 μm^2) for neat films of Y6 (A) and Y6-12 (B), each prepared from chlorobenzene and chloroform solutions. Their thickness is 60 nm for both Y6 and Y6-12 in chlorobenzene while it is 90 nm and 150 nm in chloroform, respectively.

 This journal is © The Royal Society of Chemistry 2023

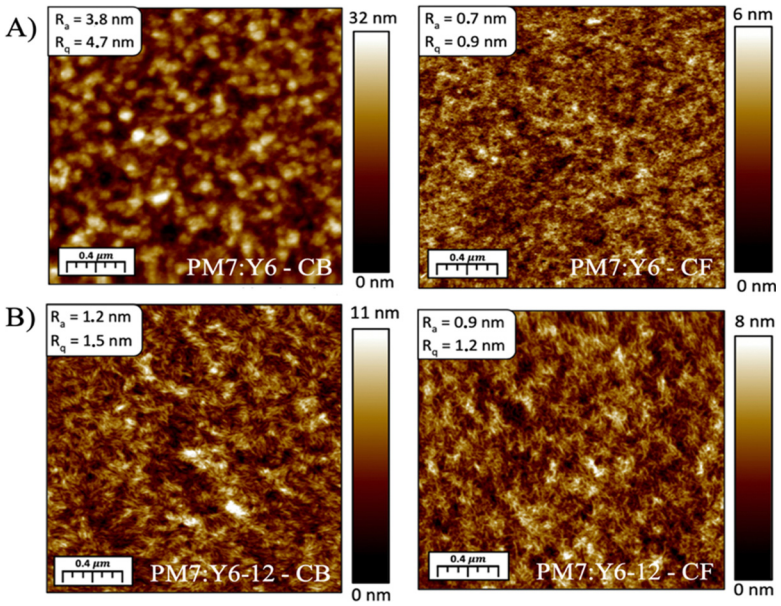

Fig. 11 AFM images (2 × 2 μm^2) for blend films of PM7:Y6 (A) and PM7:Y6-12 (B), each prepared from chlorobenzene and chloroform solutions. Their thicknesses are 105 nm and 110 nm for PM7:Y6 and PM7:Y6-12 blends in chlorobenzene while they are 98 nm and 103 nm for these films in chloroform, respectively.

value of 4.7 nm. In contrast, a 100 nm-thick blend processed from CF yields a smoother surface (R_q = 0.9 nm) without grain formation. Moreover, the film morphology of PM7:Y6 deposited from CF is very similar to that observed for PM7 alone with the same solvent; the film organization in the blend is thus driven by PM7 and attests to the good miscibility of the two components. In the case of the PM7:Y6-12 blend (Fig. 11-B), thin films of 100 nm display similar morphologies in both solvents pointing to an apparently higher degree of organization. In CB, a smooth film (R_q = 1.5 nm) and a filament-like organization driven by the polymer chains are observed. The same trends hold true in CF, except for a further decrease in rugosity (R_q = 1.2 nm). It is worth stressing that a fibril-like organization at the nanoscale is expected to favor hole transport along the polymer chains, and hence to improve the intensity of the photocurrent. In contrast, the grain morphology is expected to be a serious obstacle against efficient exciton dissociation at the donor–acceptor interface[20,61] and is thus highly detrimental to the OSC performance.

Compared to non-annealed films, the results obtained for films annealed for 10 minutes at 100 °C, as typically performed in the literature,[4,42] show similar morphologies and thicknesses, thus indicating that such an annealing post-treatment has a negligible impact on the molecular organization (see the ESI,† S3). This is, however, not the case for the neat film of Y6 and the PM7:Y6 blend prepared from CB solution. In both cases, the post-treatment leads to yet more pronounced granular morphologies with a huge increase in film thickness, from 5.1 nm to 9.9 nm for Y6 and 4.7 nm to 7.8 nm for the blend. This increase in roughness parallels the reorganization of the Y6 molecules under heat into larger grains. If applied, thermal annealing should thus be used under well-controlled conditions to avoid detrimental morphology effects, as is actually also the case for fullerene derivatives.

2.4. Device fabrication and characterization

Finally, in order to estimate the photovoltaic performance of the 100 nm-thick active layers made of PM7:Y6 and PM7 : Y6-12 in a (1 : 1) weight ratio, a series of OSCs with an inverted device architecture (Glass/ITO/Al/SnO_2/Active layer/MoO_3/Al) were fabricated and characterized, see Fig. 12. In our device architecture, a thin aluminium bus was deposited by thermal evaporation on a commercially available Indium Tin Oxide (ITO) electrode previously cleaned with soap (RBS), rinsed with distilled water, washed with acetone and isopropanol before being dried under a nitrogen flow and placed under oxygen plasma for 5 minutes. The incorporation of such a thin Al layer allows for a reduction of the series resistances (R_s) of the devices. A hole blocking layer (HBL) made of SnO_2 was then deposited from a solution containing 0.5 mL of stock solution (2.5% in weight of crystalline SnO_2 diluted in butanol) and added to 2.6 mL of butanol. This solution was spin-coated at a rotation speed of 3000 rpm for 30 seconds and an annealing step was performed by placing the sample on a hot plate for 30 min at 150 °C. All blends were spin-coated from chloroform or chlorobenzene under inert conditions at a speed of 1500 rpm for 60 sec and annealed at 100 °C for 10 minutes. An electron blocking layer (EBL) made of MoO_3 was deposited by thermal evaporation as well as the counter electrode of aluminium. All protocol steps (A), the energy diagram of the device[6,29,64,65] (B) and the thickness of each layer (C) are shown in Fig. 12. Further information about the fabrication and characterization of solar cells can be found in the ESI† (S4). The best current density–voltage (J–V) curve obtained for each active layer in both

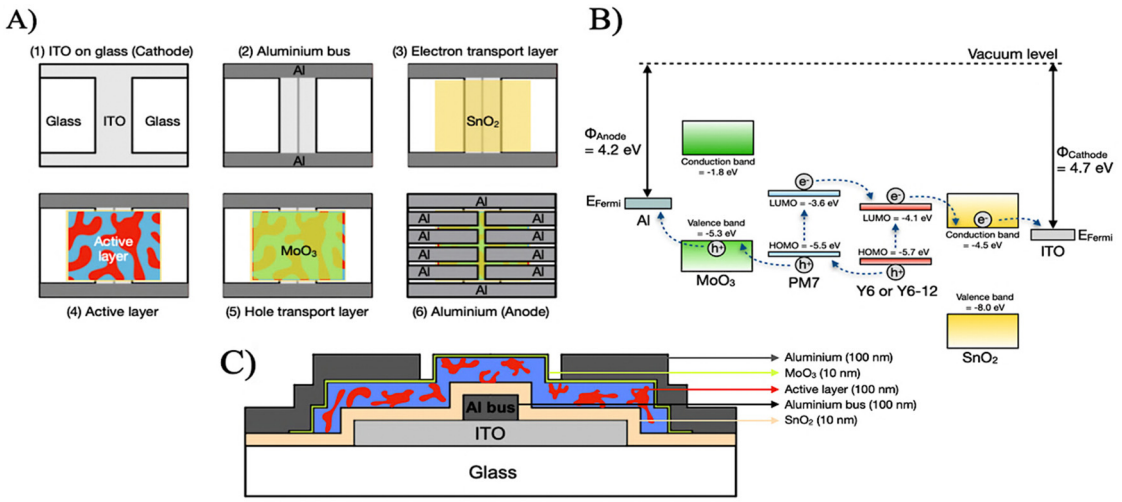

Fig. 12 Manufacturing steps (A), energy diagram (B) and side view (C) of the inverted OSC device.

solvents and their corresponding device parameters are depicted in the ESI† (S5). Table 1 summarizes the main characteristics of the fabricated solar cells with an active illuminated zone of 2.56 mm^2, as systematically averaged over 5 devices built from the same active layer (see S6, ESI†). The dispersion of the device parameters reported in the ESI† demonstrates that the consideration of 5 devices is statistically sufficient for the following discussion.

Devices made of PM7:Y6 and PM7:Y6-12 blends cast down from CF solution show similar good performances. When substituting Y6 by Y6-12, the V_{OC} value is conserved at 0.8 V, J_{SC} slightly increases from −14.6 mA cm^{-2} to −14.8 mA cm^{-2} and the FF increases from 57.2% to 59.6%, leading to maximum PCEs of 7.28% and 7.44%, respectively. The small differences in the parameter values are consistent with the good mixing of the two components observed by AFM for both mixtures deposited from chloroform. In contrast, the best OSCs including a PM7:Y6 blend prepared from a CB solution present a much lower current J_{SC} of −11.02 mA cm^{-2} compared to PM7:Y6-12 yielding a J_{SC} of −20.54 mA cm^{-2}. The V_{OC} and FF are rather similar and translate into a best PCE of 5.54% for PM7:Y6 and 11.12% for PM7:Y6-12. In this case, the side chain length has clearly a strong impact on the film morphology, as identified by AFM images pointing to the formation of grains in the PM7-Y6 blends. Since the electronic structure of Y6 and Y6-12 are expected to be very similar in thin films (as confirmed by their optical absorption spectra), the strong similarity among the V_{oc} values in Table 1 further suggests that the variation in the side chain length does not drastically affect the efficiency of the charge recombination processes. Note that an improvement in device performance when going from Y6 to Y6-12 processed from a high boiling solvent has been reported in a recent experimental study, though in combination with a different polymer (PBDB-TF-T1 terpolymer instead of PBDB-TF) and using different optimization conditions.[63]

All blends present small values of series resistances (R_{Series}) both in the dark and under illumination, thus pointing to good charge extraction and electrical contacts in the device. However, in a given solvent, the series resistances are lower for PM7:Y6 than for PM7:Y6-12. This points to a lower interface resistance between stacked layers or bulk resistance in the mixtures including Y6.[66] The values of R_{Shunt} in the dark for all blends are quite high and point to the absence of significant leakage currents. Under illumination, these values sharply decrease around 400–500 Ohm cm^2: this likely originates from the presence of energetic disorder (and hence charge carrier traps) that defines specific percolation pathways and prevents the homogeneous extraction of the charges from the active layer.[66]

The morphology changes between PM7:Y6-12 and PM7:Y6 deposited in chlorobenzene (*i.e.*, from filamentary to granular organization) impact strongly the J_{SC} parameter and decrease the PCE on an average of 5.59%. The granular morphology, probably associated with a lower solubility of Y6 in chlorobenzene promotes indeed domain sizes (∼50 to 150 nm) larger than the average exciton diffusion length (around 10–20 nm)[15] and thus not favorable for the exciton dissociation processes.

The present findings can thus be summarized in the following way: in the case of the PM7:Y6-12 blends, the solubility of both the polymer and Y6-12 are similar in CB and CF. However, during the film growth, the solvent evaporation time differs between CB and CF due to their different boiling points. In our study, the PM7:Y6-12 blend prepared from CB shows a lower R_s value, pointing to a better molecular organization when the solvent is slowly evaporating during film processing. In the case of Y6, the blends prepared from CB exhibit more pronounced aggregation than in CF, most probably because Y6 without long side chains has a large tendency to agglomerate. The use of low boiling point solvents such as CF allows for avoiding the detrimental severe aggregation of Y6, leading to better performance.

 This journal is © The Royal Society of Chemistry 2023

Table 1 Averaged cell parameter values obtained for each device manufactured in this study. All average values and their relative standard deviation are calculated for 5 devices on a single substrate

Active layer (1 : 1)	Host solvent	J_{SC} (mA cm^{-2})	V_{OC} (V)	FF (%)	$R_{Serie\ Light}$ (Ohm cm^2)	$R_{Serie\ Dark}$ (Ohm cm^2)	$R_{Shunt\ Light}$ (Ohm cm^2)	$R_{Shunt\ Dark}$ (Ohm cm^2)	Morphology	PCE (%)
PM7 : Y6	$CHCl_3$	14.04 ± 0.50	0.87 ± 0.01	56.46 ± 0.76	1.54 ± 0.17	1.60 ± 0.19	405.4 ± 10.36	46342.80 ± 20219.76	Filaments	6.91 ± 0.27
PM7 : Y6-12	$CHCl_3$	14.86 ± 0.76	0.84 ± 0.01	55.50 ± 2.41	27.58 ± 6.07	47.78 ± 12.88	445.20 ± 54.88	38181.00 ± 32358.68	Filaments	6.96 ± 0.37
PM7 : Y6	C_6H_5Cl	10.43 ± 0.41	0.82 ± 0.01	61.44 ± 0.92	0.70 ± 0.07	0.70 ± 0.07	532.20 ± 29.85	14708.80 ± 9820.29	Grains	5.25 ± 0.19
PM7 : Y6-12	C_6H_5Cl	20.43 ± 0.18	0.83 ± 0.01	63.62 ± 1.20	10.34 ± 2.94	16.00 ± 5.71	488.80 ± 16.63	5382.00 ± 1845.00	Filaments	10.84 ± 0.26

3. Conclusion

In summary, the structural and electronic properties of the widely popular NFA Y6 and its long-chain derivative Y6-12 were investigated *via* a combined theoretical and experimental approach in order to highlight the influence of the side chain elongation on the performances of OSCs. The theoretical exploration showed that the central BT unit introduced into the Y6 structure has acceptor character only when coupled to the fused pyrrole rings on each side. Simulated spectra in CF and CB pointed to weak solvatochromism which was confirmed by corresponding experimental spectra of both NFAs. The spectroscopic studies of the compounds in thin films evidenced a consequent red shift of the absorption for Y6 and Y6-12 compared to the solution, which can be attributed to pronounced electrostatic interactions in the condensed phase or to exciton delocalization upon formation of aggregates. Morphological analyses carried out by atomic force microscopy revealed no major changes in the PM7/Y6 and PM7/Y6-12 blends deposited from chloroform in contrast to the data obtained from chlorobenzene. In that case, the grain morphology and the high roughness observed for Y6 and the PM7:Y6 blend are highly detrimental for exciton dissociation processes and charge transport, leading to lower values of J_{SC} and the FF compared to the PM7:Y6-12 film promoting a significantly larger PCE. Further design of side chains together with an appropriate choice of solvent is thus clearly a route towards optimization of organic solar cells.

Conflicts of interest

There are no conflicts to declare.

Acknowledgements

The theoretical work in the Laboratory for Chemistry of Novel Materials was supported by the Consortium des 'Equipements de Calcul Intensif' funded by the Fonds National de la Recherche Scientifique (FR-FNRS) under Grant No. 2.5020.11. A. R. thanks the 'Fonds pour la Recherche Industrielle et Agricole' (FRIA) for his PhD grant. J. C. is an FNRS research director.

References

1 B. Lu, J. Wang, Z. Zhang, J. Wang, X. Yuan, Y. Ding, Y. Wang and Y. Yao, *Nano Sel.*, 2021, **2**, 2029–2039.
2 Q. Wei, W. Liu, M. Leclerc, J. Yuan, H. Chen and Y. Zou, *Sci. China: Chem.*, 2020, **60**, 1352–1366.
3 M. Riede, D. Spoltore and K. Leo, *Adv. Energy Mater.*, 2020, **11**, 2002653.
4 Y. Cui, H. Yao, L. Hong, T. Zhang, Y. Tang, B. Lin, K. Xian, B. Gao, C. An, P. Bi, W. Ma and J. Hou, *Natl. Sci. Rev.*, 2020, **7**, 1239–1246.
5 Y. Shirota and H. Kageyama, *Handbook of Organic Materials for Optical and (Opto)Electronic Devices, Properties and*

Applications, Woodhead Publishing Limited, 2013, ch. 1, pp. 3–82.
6 D. D. S. Fung and W. C. H. Choy, *Organic Solar Cells: Materials and Device Physics*, Springer-Verlag, 2013, ch. 1.
7 H. Wang, J. Cao, J. Yu, Z. Zhang, R. Geng, L. Yang and W. Tang, *J. Mater. Chem. A*, 2019, **7**, 4313–4333.
8 K. Wang, C. Liu, T. Meng, C. Yi and X. Gong, *Chem. Soc. Rev.*, 2016, **45**, 2937–2975.
9 S. Lattante, *Electronics*, 2014, **3**, 132–164.
10 J. Zhao, C. Yao, M. U. Ali, J. Miao and H. Meng, *Mater. Chem. Front.*, 2020, **4**, 3487–3504.
11 Z. Tu, G. Han and Y. Yi, *J. Phys. Chem. Lett.*, 2020, **11**, 2585–2591.
12 B. Xu, Z. Zheng, K. Zhao and J. Hou, *Adv. Mater.*, 2016, **28**, 434–439.
13 J. H. Park, T.-W. Lee, B.-D. Chin, D. H. Wang and O. O. Park, *Macromol. Rapid Commun.*, 2010, **31**, 2095–2108.
14 T.-H. Lai, S.-W. Tsang, J. R. Manders, S. Chen and F. So, *Mater. Today*, 2013, **16**, 424–432.
15 A. Uddin, *Comprehensive guide on organic and inorganic solar cells, Fundamental Concepts to Fabrication Methods*, Elsevier, 2022, ch. 1, pp. 25–55.
16 D. Qiu, M. A. Adil, K. Lu and Z. Wei, *Front. Chem.*, 2020, **8**, 603134.
17 L. Feng, J. Yuan, Z. Zhang, H. Peng, Z.-G. Zhang, S. Xu, Y. Liu, Y. Li and Y. Zou, *ACS Appl. Mater. Interfaces*, 2017, **9**, 31985–31992.
18 S. Zhong, B. Kar Yap, Z. Zhong and L. Ying, *Crystals*, 2022, **12**, 168.
19 P. Cheng, G. Li, X. Zhan and Y. Yang, *Nat. Photonics*, 2018, **12**, 131–142.
20 D. Li, X. Zhang, D. Liu and T. Wang, *J. Mater. Chem. A*, 2020, **8**, 15607–15619.
21 J. Yang, Y. Geng, J. Li, B. Zhao, Q. Guo and E. Zhou, *J. Phys. Chem. C*, 2020, **124**, 24616–24623.
22 H. Chung, J. Oh, J.-H. Park, I. Cho, W. S. Yoon, J. E. Kwon, D. Kim and S. Y. Park, *J. Phys. Chem. C*, 2020, **124**, 18502–18512.
23 B. Kan, Y. Kan, L. Zuo, X. Shi and K. Gao, *InfoMat*, 2020, **3**, 175–200.
24 C. K. Luscombe, U. Maitra, M. Walter and S. K. Wiedmer, *Chem. Teach. Int.*, 2020, **3**, 1–15.
25 S. Dai, Y. Xiao, P. Xue, J. J. Rech, K. Liu, Z. Li, X. Lu, W. You and X. Zhan, *Chem. Mater.*, 2018, **30**, 5390–5396.
26 J. Yuan, Y. Zhang, L. Zhou, G. Zhang, H.-L. Yip, T.-K. Lau, X. Lu, C. Zhu, H. Peng, P. A. Johnson, M. Leclerc, Y. Cao, J. Ulanski, Y. Li and Y. Zou, *Joule*, 2019, **3**, 1140–1151.
27 Z. Zhang, Y. Wang, C. Sun, Z. Liu, H. Wang, L. Xue and Z.-G. Zhang, *Nano Sel.*, 2021, **3**, 233–247.
28 S. Dey, *Small*, 2019, **15**, 1900134.
29 S. Li, C.-Z. Li, M. Shi and H. Chen, *ACS Energy Lett.*, 2020, **5**, 1554–1567.
30 Y. Chen, R. Ma, T. Liu, Y. Xiao, H. K. Kim, J. Zhang, C. Ma, H. Sun, F. Bai, X. Guo, K. S. Wong, X. Lu and H. Yan, *Adv. Energy Mater.*, 2021, **11**, 200377.
31 X. Kong, J. Zhang, L. Meng, C. Sun, S. Qin, C. Zhu, J. Zhang, J. Li, Z. Wei and Y. Li, *CCS Chem.*, 2022, **0**, 1–10.
32 M. Li, P. J. Leenaers, M. M. Wienk and R. A. J. Janssen, *J. Mater. Chem. C*, 2020, **8**, 5856–5867.
33 S.-C. Lan, C.-K. Chang, Y.-H. Lu, S.-W. Lin, A. K. Y. Jen and K.-H. Wei, *RSC Adv.*, 2015, **5**, 67718.
34 L. Wang, C. Guo, X. Zhang, S. Cheng, D. Li, J. Cai, C. Chen, Y. Fu, J. Zhou, H. Qin, D. Liu and T. Wang, *Chem. Mater.*, 2021, **33**, 8854–8862.
35 K. Jiang, Q. Wei, J. Y. L. Lai, Z. Peng, H. K. Kim, J. Yuan, L. Ye, H. Ade, Y. Zou and H. Yan, *Joule*, 2019, **3**, 3020–3033.
36 Z. Luo, R. Sun, C. Zhong, T. Liu, G. Zhang, Y. Zou, X. Jiao, J. Min and C. Yang, *Sci. China: Chem.*, 2020, **63**, 361–369.
37 J. Wang, X. Jiang, H. Wu, G. Feng, H. Wu, J. Li, Y. Yi, X. Feng, Z. Ma, W. Li, K. Vandewal and Z. Tang, *Nat. Commun.*, 2021, **12**, 6679.
38 O. A. Vydrov and G. E. Scuseria, *J. Chem. Phys.*, 2006, **125**, 234109.
39 C. Risko and J.-L. Brédas, *Multiscale Modelling of Organic and Hybrid Photovoltaics*, Springer, 2013, ch. 1, pp. 1–38.
40 E. Chigo-Anota, M. A. Alejandro, A. B. Hernàndez, J. J. S. Torres and M. Castro, *RSC Adv.*, 2016, **6**, 20409.
41 M. Frisch, G. Trucks, J. Cheeseman, *et al.*, *Gaussian 16 Rev. A.03 Release Notes*, 2017. https://gaussian.com/relnotes_a03/.
42 Y. Cui, H. Yao, J. Zhang, T. Zhang, Y. Wang, L. Hong, K. Xian, B. Xu, S. Zhang, J. Peng, Z. Wei, F. Gao and J. Hou, *Nat. Commun.*, 2019, **10**, 2515.
43 B. Mennucci, *Wiley Interdiscip. Rev. Comput. Mol. Sci.*, 2012, **2**, 386–404.
44 B. Mennucci, J. Tomasi, R. Cammi, J. R. Cheeseman, M. J. Frisch, F. J. Devlin, S. Gabriel and P. J. Stephens, *J. Phys. Chem. A*, 2002, **106**, 6102–6113.
45 F. Lipparini, G. Scalmani, B. Mennucci and M. J. Frisch, *J. Chem. Theory Comput.*, 2011, **7**, 610–617.
46 J. Cornil, I. Gueli, A. Dkhissi, J. C. Sancho-Garcia, E. Hennebicq, J. P. Calbert, V. Lemaur, D. Beljonne and J.-L. Brédas, *J. Chem. Phys.*, 2003, **118**, 6615.
47 G. Han, T. Hu and Y. Yi, *Adv. Mater.*, 2020, **32**, 2000975.
48 G. Londi, R. Dilmurat, G. D'Avino, V. Lemaur, Y. Olivier and D. Beljonne, *Phys. Chem. Chem. Phys.*, 2019, **21**, 25023–25034.
49 S. H. Park, N. Y. Kwon, H. J. Kim, E. Cho, H. Kang, A. K. Harit, H. Y. Woo, H. J. Yoon, M. J. Cho and D. H. Choi, *ACS Appl. Mater. Interfaces*, 2021, **13**, 13487–13498.
50 M. Picollo, M. Aceto and T. Vitorino, *Phys. Sci. Rev.*, 2018, **0**, 1–14.
51 H. Itagaki, *Experimental Methods in Polymer Science – Modern methods in Polymer, Research and Technology*, Elsevier Inc., 2000, ch. 3, pp. 155–260.
52 J. Yan, X. Rodrìguez-Martìnez, D. Pearce, H. Douglas, D. Bili, M. Azzouzi, F. Eisner, A. Virbule, E. Rezasoltani, V. Belova, B. Dörling, S. Few, A. A. Szumska, X. Hou, G. Zhang, H.-L. Yip, M. Campoy-Quiles and J. Nelson, *Energy Environ. Sci.*, 2022, **15**, 2958.
53 X. Jiang, P. Chotard, K. Luo, F. Eckmann, S. Tu, M. A. Reus, S. Yin, J. Reitenbach, C. L. Weindl, M. Schwartzkopf and S. V. Roth, *Adv. Energy Mater.*, 2022, **12**, 2103977.

 This journal is © The Royal Society of Chemistry 2023

54 A. Casey, S. D. Dimitrov, P. Shakya-Tuladhar, Z. Fei, M. Nguyen, Y. Han, T. D. Anthopoulos, J. R. Durrant and M. Heeney, *Chem. Mater.*, 2016, **28**, 5110–5120.
55 J. Cornil, D. A. dos Santos, X. Crispin, R. Silbey and J.-L. Brédas, *J. Am. Chem. Soc.*, 1998, **120**, 1289–1299.
56 M. Li, H. Bin, X. Jiao, M. M. Wienk, H. Yan and R. A. J. Janssen, *Angew. Chem., Int. Ed.*, 2019, **59**, 846–852.
57 H. Bässler and B. Schweitzer, *Acc. Chem. Res.*, 1999, **32**, 173–182.
58 M. Kasha, *Radiat. Res.*, 1963, **20**, 55–70.
59 G. D'Avino, L. Muccioli, F. Castet, C. Poelking, D. Andrienko, Z. G. Soos, J. Cornil and D. Beljonne, *J. Phys.: Condens. Matter*, 2016, **28**, 433002.
60 S. Mahjabin, M. M. Haque, S. Khan, V. Selvanathan, M. S. Jamal, M. S. Bashar, H. I. Alkhammash, M. I. Hossain, M. Shahiduzzaman, N. Amin, K. Sopian and M. Akhtaruzzaman, *Sol. Energy*, 2021, **222**, 202–211.
61 L. Ma, Y. Xu, Y. Zu, Q. Liao, B. Xu, C. An, S. Zhang and J. Hou, *Sci. China: Chem.*, 2020, **63**, 21–27.
62 S. Zhang, Y. Qin, J. Zhu and J. Hou, *Adv. Mater.*, 2018, **30**, 1800868.
63 L. Hong, H. Yao, Z. Wu, Y. Cui, T. Zhang, Y. Xu, R. Yu, Q. Liao, B. Gao, K. Xian, H. Y. Woo, Z. Ge and J. Hou, *Adv. Mater.*, 2019, **31**, 1903441.
64 T. Hori, H. Moritou, N. Fukuoka, J. Sakamoto, A. Fujii and M. Ozaki, *Materials*, 2010, **3**, 4915–4921.
65 J. Song, E. Zheng, X.-F. Wang, W. Tian and T. Miyasaka, *Sol. Energy Mater. Sol. Cells*, 2016, **144**, 623–630.
66 B. Qi and J. Wang, *Phys. Chem. Chem. Phys.*, 2013, **15**, 8972.

This journal is © The Royal Society of Chemistry 2023